Article

# Rapid and Reversible Lithium Insertion in the Wadsley−Roth-Derived Phase NaNb$_{13}$O$_{33}$

Ashlea R. Patterson, Rodrigo Elizalde-Segovia, Kira E. Wyckoff, Arava Zohar, Patrick P. Ding, Wiley M. Turner, Kenneth R. Poeppelmeier, Sri R. Narayan, Raphaële J. Clément, Ram Seshadri, and Kent J. Griffith*

Read Online

ACCESS | Metrics & More | Article Recommendations | SI Supporting Information

**ABSTRACT:** The development of new high-performing battery materials is critical for meeting the energy storage requirements of portable electronics and electrified transportation applications. Owing to their exceptionally high rate capabilities, high volumetric capacities, and long cycle lives, Wadsley−Roth compounds are promising anode materials for fast-charging and high-power lithium-ion batteries. Here, we present a study of the Wadsley−Roth-derived NaNb$_{13}$O$_{33}$ phase and examine its structure and lithium insertion behavior. Structural insights from combined neutron and synchrotron diffraction as well as solid-state nuclear magnetic resonance (NMR) are presented. Solid-state NMR, in conjunction with neutron diffraction, reveals the presence of sodium ions in perovskite A-site-like block interior sites as well as square-planar block corner sites. Through combined experimental and computational studies, the high rate performance of this anode material is demonstrated and rationalized. A gravimetric capacity of 225 mA h g$^{-1}$, indicating multielectron redox of Nb, is accessible at slow cycling rates. At a high rate, 100 mA h g$^{-1}$ of capacity is accessible in 3 min for micrometer-scale particles. Bond-valence mapping suggests that this high-rate performance stems from fast multichannel lithium diffusion involving octahedral block interior sites. Differential capacity analysis is used to identify optimal cycling rates for long-term performance, and an 80% capacity retention is achieved over 600 cycles with 30 min charging and discharging intervals. These initial results place NaNb$_{13}$O$_{33}$ within the ranks of promising new high-rate lithium-ion battery anode materials that warrant further research.
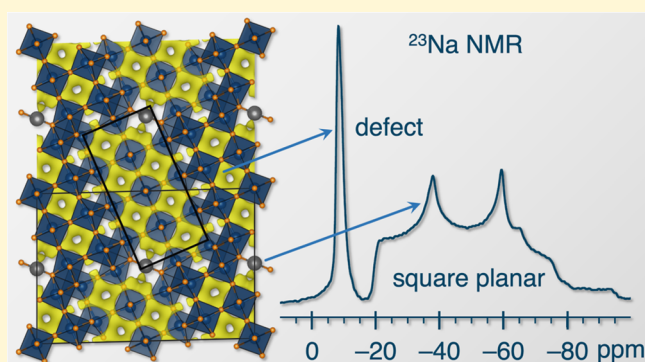
## INTRODUCTION

As we transition from fossil fuels to low-carbon energy sources, faster charging, higher energy, and higher power lithium-ion batteries (LIBs) are required to support widespread electrification. LIBs typically use graphitic carbon as the anode material given its high lithium storage capacity, low cost, and low voltage vs Li$^+$/Li, which leads to a high energy density when paired with a 4-V-class cathode material such as Li(Ni,Mn,Co,Al)O$_2$.[1,2] However, the low voltage of graphite lithiation relative to the lithium metal deposition potential can lead to electrolytic side reactions and lithium metal plating, the results of which are increased impedance, shortened battery lifetimes, and thermal runaway should lithium dendrites traverse the separator.[3−5] These issues, which are especially problematic at high current densities, have motivated the search for alternative anode materials that operate between 1.0 and 2.0 V vs Li$^+$/Li.[6,7]

Wadsley−Roth compounds are a family of (mostly) transition metal oxides that have garnered interest as fast-charging LIB anodes. Many of these compounds were first reported in the 1950s−1960s[8−13] but were not considered as

electrode materials until the seminal work of Cava et al.[14−16] Research into Wadsley−Roth electrodes declined until two 2011 papers by Han, Goodenough, and colleagues demonstrated excellent rate performance, respectable capacities, and stable cycling with the Wadsley−Roth phase TiNb$_2$O$_7$ as a lithium intercalation anode.[6,7] Wadsley−Roth compounds typically operate above 0.8 V vs Li$^+$/Li and are thus not subject to lithium plating or deleterious side reactions with the electrolyte. They also tend to insert more than one lithium per transition metal with a minor volume expansion. This allows for large and reversible lithium storage capacities and good long-term electrochemomechanical stability. Finally, Wadsley−Roth anodes have demonstrated excellent high-rate performance.[6,7,17−21]
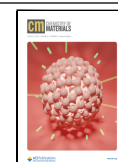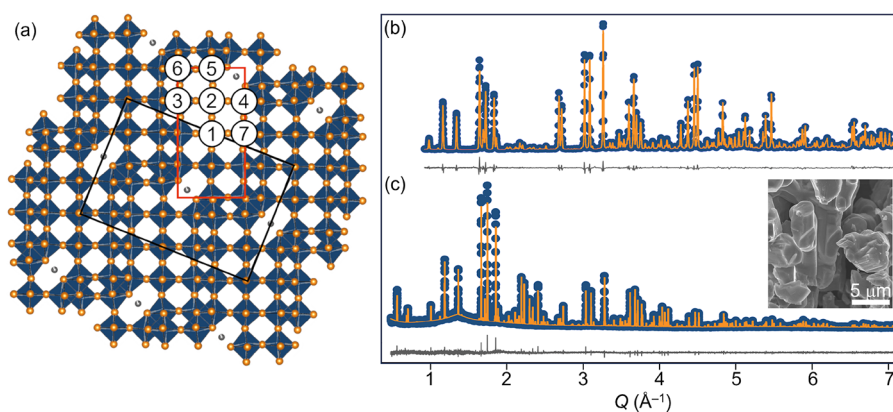
**Figure 1.** (a) Schematic of the $NaNb_{13}O_{33}$ crystal structure highlighting the $(5\times3-2)_\infty$ blocks of $NbO_6$ octahedra and each unique Nb site. (b) Neutron powder diffraction of 1-NNO obtained at 300 K, $\lambda_c = 1.5$ Å. (c) Synchrotron X-ray powder diffraction of 1-NNO at 300 K, $\lambda_c = 0.45788$ Å. The diffuse background feature is due to the Kapton capillary sample holder. The inset shows an SEM image of pristine 1-NNO particles

Wadsley–Roth compounds are characterized by $m \times n$ blocks of corner-sharing $MO_6$ octahedra joined by edge-sharing octahedra in "shear" planes, as first described by Roth in 1965.[9,10] Unlike one-dimensional shear structures and layered vacancy-ordered Wadsley–Roth derivatives that exhibit relatively poor capacity retention upon electrochemical cycling,[22-24] Wadsley–Roth phases exhibit good stability upon repeated lithium (de)intercalation because of the structural rigidity and minimal volume expansion imparted by the shear planes.[18,25-28] Moreover, a combination of experimental and computational studies on Wadsley–Roth phases have provided evidence for rapid, quasi-one-dimensional lithium diffusion down parallel octahedral block channels paired with facile interchannel hopping, which helps to redistribute lithium and prevent blockages.[26,29,30] This combination of long-range diffusion and short-range redistribution accounts for the extremely high lithium diffusion coefficients reported for Wadsley–Roth electrodes, which are on par with those of lithium-conducting solid electrolytes.[18,19,31] Additional studies have shown good electronic conductivity in Wadsley–Roth phases once they are partially reduced by either oxygen loss or lithium insertion.[14,29,32-34] This rapid intercalation behavior has been observed in micrometer-scale particles, indicating that Wadsley–Roth phases do not require nanostructuring for high-rate performance.

The present study comprises an in-depth structural and initial electrochemical investigation of the Wadsley–Roth-like phase $NaNb_{13}O_{33}$. The structure of this composition within the $Nb_2O_5$–$Na_2O$ solid solution system was first reported in 1965.[35] Its block-defect structure and sodium conductivity were investigated in 1984,[36] and its thermodynamic stability has been the subject of several reports.[37-39] This compound deviates from the typical Wadsley–Roth structure in that transition-metal-centered octahedra are missing from the corners of the blocks, and instead, sodium ions occupy square planar sites. This is a relatively rare $Na^+$ coordination that results in large rectangular tunnels connecting the Na sites. Following the $(m \times n)_\infty$ Wadsley–Roth nomenclature where $m$ and $n$ are the block dimensions in units of octahedra and the subscript denotes the connectivity of the blocks in the block plane, we propose that the deviation in $NaNb_{13}O_{33}$ should be denoted $(5\times3-2)_\infty$ (Figure 1a).

We report structural insights from combined neutron and synchrotron diffraction of $NaNb_{13}O_{33}$ along with $^{23}Na$ solid-

state nuclear magnetic resonance spectroscopy. A new picture of the atomic-scale defect structure emerges with sodium cations occupying not only the square-planar sites but also perovskite-like sites within the block interiors. Density functional theory calculations of the electronic structure and bond-valence sum mapping of the electrostatic landscape suggest good electronic and ionic conductivity. This is confirmed by the electrochemical behavior of this material in Li half-cell batteries, which reveal excellent rate capability and long-term cyclability with micrometer-sized $NaNb_{13}O_{33}$ particles. Finally, galvanostatic cycling suggests Nb multi-electron redox, which enables large amounts of lithium to be stored in this promising new anode material.

## METHODS

**Solid-State Synthesis of $NaNb_{13}O_{33}$.** $NaNb_{13}O_{33}$ was prepared by multiple independent solid-state methods. In the first preparation method, resulting in the sample hereafter termed 1-NNO, $Nb_2O_5$ (CBMM, 99.8%, white powder, 1:1 T-phase:H-phase) and $Na_2CO_3$ (Sigma, 99.95–100.05%, anhydrous, white powder, dried at 250 °C for 8 h) were hand-mixed and ground in an agate mortar and pestle for 10 min before being pressed into two 5 g, 25.4 mm diameter pellets at 300 MPa. The pellets were placed in a Pt crucible and fired in a three-stage heating program, all with 5 °C min$^{-1}$ heating rates, at 400 °C for 6 h, 820 °C for 12 h, and 1150 °C for 18 h before being cooled in the furnace under zero power. Note that the sample prepared for synchrotron diffraction used a single heating step at 1150 °C for 24 h.

In the second solid-state preparation method, which resulted in the sample termed 2-NNO, $NaNbO_3$ was first prepared by hand-grinding a 1:1 molar ratio of $Nb_2O_5$ (Materion, ≥99%) and $Na_2CO_3$ (Sigma, ≥99%) in an agate mortar and pestle for 20 min. The resulting mixture was pressed into 700 mg, 13 mm pellets under 3.5 t of pressure. Pellets were placed on a bed of sacrificial powder within an alumina crucible, heated to 1100 °C at a rate of 10 °C min$^{-1}$, sintered for 12 h, and then air-quenched. The same grinding, pelletizing, heating, and quenching procedure was then repeated to produce $NaNb_{13}O_{33}$ from a hand-ground mixture of $NaNbO_3$ and $Nb_2O_5$ in a 1:6 molar ratio.

**Scanning Electron Microscopy (SEM).** To characterize the morphology and size of 1- and 2-NNO particles, $NaNb_{13}O_{33}$ pellets were hand-ground for approximately 10 min in an agate mortar and pestle. The powdered samples were then pressed onto double-sided carbon tape and measured with a Hitachi S4800 (1-NNO) or an Apreo C FEG (ThermoFisher) (2-NNO) microscope. SEM images were collected using secondary electron (SE) detection with 10 kV accelerating voltage.

**Diffraction.** Synchrotron X-ray powder diffraction (SXRPD) data were collected on both 1- and 2-NNO at 300 K on the 11-BM beamline at the Advanced Photon Source at Argonne National Laboratory with a wavelength $\lambda$ = 0.45788 Å. Time-of-flight neutron powder diffraction (TOF-NPD) data of 1-NNO were obtained on the POWGEN diffractometer at the Spallation Neutron Source (SNS) located at Oak Ridge National Laboratory.[40] Approximately 10 g of $NaNb_{13}O_{33}$ was loaded into an 8 mm diameter cylindrical vanadium can. Data were collected on POWGEN detector bank 2 with a center wavelength of 1.5 Å at 20 and 300 K with scan times of 75 and 95 min, respectively, and detector bank 3 with a center wavelength of 2.665 Å at 300 K for 5 min. Combined Rietveld analysis on SXRPD and TOF-NPD data was performed using GSAS-II.[41] Fitting information and refined patterns of both samples are included in the Supporting Information (S1−S2).

**Nuclear Magnetic Resonance (NMR).** To better understand the local structure of as-prepared $NaNb_{13}O_{33}$, magic-angle spinning (MAS) solid-state $^{23}Na$ NMR was performed on 1- and 2-NNO compounds at room temperature.

Solid-state $^{23}Na$ MAS NMR spectra were acquired on 1-NNO using a Bruker AVANCE III 400 MHz (9.4 T) spectrometer and a 1.6 mm Phoenix HX MAS probe or a 4 mm Bruker HX MAS probe. The 1-NNO sample was packed into zirconia rotors in air and rotated about the magic angle at 12.5 kHz to obtain high signal-to-noise spectra using a 4 mm rotor and at 38 kHz for the variable-temperature study using a 1.6 mm rotor. One-pulse spectra were collected using an rf pulse of either 0.8 μs (1.6 mm probe) or 1.3 μs (4 mm probe), corresponding to half the length of a liquid-state $^{23}Na$ $\pi/2$ pulse to account for the doubling of the nutation frequency of this spin-3/2 nucleus in the solid state. $T_1$ values were measured with a saturation−recovery pulse sequence, and recycle delays were subsequently set to 5 × $T_1$. For comparison, spectra of $NaNbO_3$ and $Na_{13}Nb_{35}O_{94}$ were obtained using similar data acquisition parameters. $^{23}Na$ shifts of 1-NNO, $NaNbO_3$, and $Na_{13}Nb_{35}O_{94}$ were referenced to aqueous 1.0 M NaCl at 0 ppm. Actual sample temperatures during variable-temperature MAS NMR data acquisition differ from the value measured by the thermocouple due to frictional heating of the sample. The sample temperature was externally calibrated by leveraging the temperature dependence of the $^{207}Pb$ shift of a lead nitrate reference sample.[42,43] A solid-state $^{23}Na$ MAS NMR spectrum of the 2-NNO material was also acquired, as detailed in the Supporting Information.

**Electronic Structure and Bond Valence Sum Calculations.** To understand the electronic properties of the host structure, density functional theory (DFT) calculations were performed using the Vienna Ab initio Simulation Project (VASP)[44−46] code, projector augmented-wave (PAW) pseudopotentials,[47,48] and the general-gradient-approximation Perdew−Burke−Ernzerhof (PBE)[49] functional. Structural models were obtained from a joint refinement of 1-NNO neutron and synchrotron XRD diffraction patterns obtained at 20 K. Lattice parameters and atomic positions were optimized by using a plane-wave energy cutoff of 500 eV and a $k$-point mesh with a length-density parameter of $R_k$ = 25 Å, corresponding to a 7 × 2 × 2 Γ-centered mesh. Structural relaxation was followed by static calculations of the projected density of states (DOS) and electronic band structure, which was postprocessed using the Sumo package.[50]

To estimate the pathways for ion intercalation in the three-dimensional $NaNb_{13}O_{33}$ host structure, bond valence sum mapping was performed with either $Li^+$ or $Na^+$ as the mobile ion using softBV-GUI ver. 1.2.7.[51−53] Energy barriers for ion hopping within the $NaNb_{13}O_{33}$ unit cell were visualized in VESTA[54] using an isosurface energy cutoff of 0.1 valence units.

Finally, DFT, as implemented in plane wave code CASTEP v19.11, was used to compute the quadrupolar tensor of $NaNb_{13}O_{33}$. The calculations were performed using "on-the-fly" ultrasoft pseudopotentials and the PBE exchange−correlation functional.[49,55−57] The plane-wave basis set was truncated at an energy cutoff of 700 eV, and integration over reciprocal space was performed using a 2 × 7 × 2 Monkhorst−Pack grid.[58] Structures were geometry optimized prior to NMR calculations.[59−61] Spectral simulations of the calculated quadrupolar tensor were performed with the Solid Lineshape Analysis (SOLA) tool in TopSpin v4.0.9.

**Electrochemical Characterization.** Electrodes composed of 2-NNO, Super P carbon black, and poly(vinylidene difluoride) (PVDF) were fabricated in a weight ratio of 80:10:10. Pristine 2-NNO was blended with carbon black (MTI Super P) in a mortar and pestle and mixed into a solution of PVDF (MTI) in N-methyl-2-pyrrolidone (NMP, Sigma-Aldrich, 40 g $L^{-1}$) to produce a slurry. The slurry was cast onto copper foil using a doctor blade, giving a coating thickness of approximately 40 μm. The resulting film was vacuum-dried at 80 °C overnight and punched into 14 mm diameter discs, resulting in approximate active material mass loadings of 2.0−5.5 mg $cm^{-2}$. The electrodes were incorporated into CR2032 coin cells from MTI in an argon-filled glovebox, with polished lithium metal (MTI) as a counter electrode and glass fiber separators (Whatman GF/C). An electrolyte of 1.0 M lithium bis(trifluoromethanesulfonyl)imide (LiTFSI, Sigma-Aldrich) dissolved in 1:1 v/v ethylene carbonate (EC, Sigma-Aldrich) and dimethyl carbonate (DMC, Sigma-Aldrich) was added to the cell in a ratio of 25 μL of electrolyte per milligram of active material. Half-cells of 2-NNO electrodes vs sodium metal were fabricated in a similar manner, as detailed in the Supporting Information.

On the basis of reduction of $Nb^{5+}$ to $Nb^{4+}$, 13 Li or Na ions inserted into $NaNb_{13}O_{33}$ would yield a theoretical capacity of 198 mA h $g^{-1}$ based on the molecular mass of the pristine compound as is standard for anode materials. Cycling rate is defined as C/$n$, where $n$ is the number of hours to complete a single charge or discharge. Therefore, a C/10 rate corresponds to the current density needed to fully charge or discharge to the theoretical capacity in 10 h or a current density of 19.8 mA $g^{-1}$. All electrochemical experiments were performed using Biologic potentiostats.

# ■ RESULTS AND DISCUSSION

**Characterization of the $NaNb_{13}O_{33}$ Host Structure.** Scanning electron microscopy (SEM) images of pristine 1-NNO show particles on the order of 5−50 μm, while SEM images of 2-NNO show particles on the order of 1−10 μm (Figure 1 inset and Figure S4). Synchrotron powder X-ray diffraction (SXPRD) and neutron powder diffraction (NPD) patterns were collected and jointly refined to examine phase purity, octahedral distortions, and sodium position(s) and occupancy(ies) in $NaNb_{13}O_{33}$. X-ray diffraction confirms the phase purity of the $NaNb_{13}O_{33}$ samples prepared using the two synthesis methods (Figures 1c and S2). Neutron diffraction gives atomic displacement parameters (ADPs) for each Nb and Na site within the structure at 20 and 300 K (Figure 1b). Square-planar Na shows a relatively large atomic displacement parameter (ADP) at room temperature, indicating greater motion of the $Na^+$ ions around their nominal positions in the crystal structure. ADPs and second-order Jahn−Teller distortion parameters for the $NbO_6$ octahedra are listed in Table S1.

$^{23}Na$ solid-state MAS NMR of $NaNb_{13}O_{33}$ revealed two environments (Figure 2, black curve): a sharp resonance at −8 ppm and a broad resonance centered at −50 ppm, with respective relative integrated intensities of 16:84. The $T_1$ relaxation times of the high- and low-frequency components are 3.1 and 0.91 s, respectively. The relaxation difference is sensible given that the low-frequency resonance has a larger quadrupolar interaction, and quadrupolar relaxation is expected to be the dominant relaxation mechanism for $^{23}Na$ in diamagnetic $NaNb_{13}O_{33}$. This low-frequency resonance, with an isotropic shift of −15 ppm, a large quadrupolar coupling constant of $C_Q$ = 3.74 MHz, and asymmetry $\eta_Q$ = 0.42 (Figure 2, blue curve), corresponds to a spherically asymmetric Na site. It is therefore assigned to the square-planar coordinated Na site in the $NaNb_{13}O_{33}$ crystal structure. The
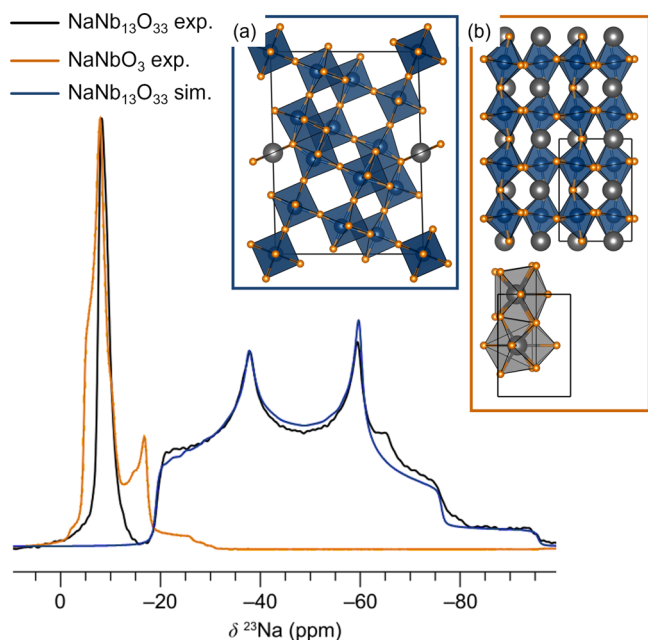
**Figure 2.** $^{23}$Na MAS NMR of 1-NNO featuring two distinct resonances (black curve): a fit of the quadrupolar environment with a center of mass at approximately −50 ppm (blue curve) and an overlaid experimental spectrum of NaNbO$_3$ (orange curve). Spectra were acquired at room temperature at 9.4 T and 12.5 kHz MAS. Box (a) shows the NaNb$_{13}$O$_{33}$ structure with its square-planar Na environment, which is assigned to the strongly quadrupolar line shape, while box (b) shows the Na environments in NaNbO$_3$. Grey spheres and polyhedra correspond to sodium, blue octahedra are NbO$_6$.

quadrupolar parameters measured for this Na site, and particularly the magnitude of the quadrupolar coupling, are in good agreement with results from CASTEP NMR calculations ($C_Q$ = 3.96 MHz; $\eta_Q$ = 0.13) on the Na-ordered parent structure.

The sharp Na environment, however, cannot be explained by the Na-ordered pristine NaNb$_{13}$O$_{33}$ structure with its single square-planar Na coordination. Curiously, it is consistent with the presence of Na in the 12-coordinate site within the octahedral block channels (i.e., the perovskite A-site) of this Wadsley−Roth-derived phase. A Na atom occupying this perovskite-like site within NaNb$_{13}$O$_{33}$ would have a mean distance from the 12 nearest atoms of 2.82 Å, which is quite similar to that of NaNbO$_3$, and indeed, the chemical shift is virtually identical with that of Na in perovskite NaNbO$_3$ (Figure 2, orange curve). However, no secondary phase of NaNbO$_3$ was observed in either high-resolution SXRPD or NPD, and the line shape of the sharp resonance in the NaNb$_{13}$O$_{33}$ sample is narrower than that observed in any of the polymorphs of NaNbO$_3$.[62,63] The narrower resonance could be the result of (i) fast local Na dynamics or (ii) a less distorted Na local environment in NaNb$_{13}$O$_{33}$—or perhaps a combination of both.

In NaNbO$_3$, the Na sites are highly distorted (Figure 2b).[64] With a Goldschmidt tolerance factor less than one, NbO$_6$ octahedra in NaNbO$_3$ may tilt and rotate around the Na sites, while second-order Jahn−Teller distortions associated with Nb$^{5+}$ add to the asymmetry. Conversely, the presence of significant edge-sharing in NaNb$_{13}$O$_{33}$ prevents octahedral rotation and tilting, and the occupancy of sodium on the

perovskite A-site position in NaNb$_{13}$O$_{33}$ is far less than unity (vide infra), which will affect electrostatic repulsion. Hence, Na ions in the perovskite-like sites of NaNb$_{13}$O$_{33}$ are expected to be in more symmetrical environments than those in NaNbO$_3$.

Overall, there is evidence to suggest that the additional NMR resonance should be attributed to a fraction of Na in the interstitial, perovskite A-site-like positions of NaNb$_{13}$O$_{33}$ rather than an impurity phase such as NaNbO$_3$. This idea is supported by further evidence from diffraction. First, in the joint refinement, the occupancy of Na in the square-planar site freely refines to 0.85(4) at 20 K and 0.89(2) at 300 K, which are within error and similar to the 84% integrated NMR signal intensity obtained for the low-frequency component of 1-NNO (87% for 2-NNO (Figure S3)). We note that there are challenges to the precise quantification of NMR signal intensities of sites with significantly different quadrupolar coupling interaction magnitudes.[65] In the case of a spin-3/2 nucleus such as $^{23}$Na, 60% of the total intensity is contained in the satellite transitions[66] that are expected to be distributed over the spinning sidebands for the highly quadrupolar square-planar site but would be expected to be partially or fully folded into the sharp centerband of the perovskite-like site. Thus, a reasonable bound on the relative sodium occupancies from these data sets would be 84%−93% for the broad low-frequency signal and 7%−16% for the narrow high-frequency signal.

Second, Fourier difference maps of the neutron diffraction data at 20 K reveal nuclear density near the center of the perovskite-like sites in NaNb$_{13}$O$_{33}$ (Figure S9). The data are too noisy to yield accurate refined Na occupations or ADPs within each perovskite-like site, which is not surprising given that there is only one Na per NaNb$_{13}$O$_{33}$ formula unit, and there are six such sites that are expected to sum to 7%−16% of the Na, so the occupancies may only be around 1%−2% per site. Neutron diffraction was helpful here because the relative scattering of Na vs Nb is roughly 1:2 with neutrons, compared to 1:4 with X-rays, and because nuclear density is less diffuse than electron density.

The third and final piece of evidence for this assignment of the NMR data, and for the presence of point defects in NaNb$_{13}$O$_{33}$, comes from phase boundary mapping.[67,68] With this technique, the target compound NaNb$_{13}$O$_{33}$ is purposefully made off-stoichiometric on the Na-poor side and the Na-rich side of the phase diagram until a secondary phase appears. In the case of NaNb$_{13}$O$_{33}$ prepared under the 1-NNO synthesis conditions, the adjacent Na-poor phase is H−Nb$_2$O$_5$ and the adjacent Na-rich phase is the bronze-like phase Na$_{13}$Nb$_{35}$O$_{94}$. With excess Nb$_2$O$_5$ added to the synthesis, reflections from H−Nb$_2$O$_5$ are clearly visible in the XRD pattern, and there is nearly no change in the $^{23}$Na NMR spectrum (Figures S6 and S7), suggesting that the Na-containing phase is unaffected. With excess Na$_2$CO$_3$ added to the synthesis, small Bragg reflections from the bronze-like phase become visible in XRD, and significant $^{23}$Na NMR signal intensity appears around −22 ppm, along with broadening around the base of the signal at −8 ppm (Figure S6). A spectrum of pure Na$_{13}$Nb$_{35}$O$_{94}$ reveals a strong resonance at −22 ppm and a weaker resonance at −8 ppm that is four times broader than the sharp signal at −8 ppm in NaNb$_{13}$O$_{33}$ (Figure S6). The crystal structure of Na$_{13}$Nb$_{35}$O$_{94}$ contains four unique sodium sites, with two in four-sided tunnels, much like the perovskite-like site in NaNb$_{13}$O$_{33}$, and two in pentagonal tunnels that are common in bronze-like compounds. Although

it goes beyond the scope of this work, we propose that the resonance at −8 ppm in $Na_{13}Nb_{35}O_{94}$ originates from the perovskite A-cation-like site, which would be consistent with those of $NaNb_{13}O_{33}$ and $NaNbO_3$.

Taken together, the structural data show that $NaNb_{13}O_{33}$ contains approximately 90% Na on the square-planar site with 10% distributed onto the perovskite A-site-like environments within the $(5×3−2)_\infty$ blocks of $NbO_6$ octahedra.

Near-ambient Na dynamics were investigated with variable-temperature $^{23}$Na NMR (Figure S8). The spectra collected from −13 to 72 °C are nearly temperature-independent. A small drift in the resonance frequency is observed, but no appreciable line-broadening occurs across the temperatures measured. At low temperatures, no additional environments appear, indicating that the $Na^+$ ions have not been "frozen out", and at elevated temperatures, the line widths do not narrow or merge, indicating no appreciable chemical exchange between Na sites. Bovin's study of $NaNb_{13}O_{33}$ reported $Na^+$-ion conductivities from $6 × 10^{-2}$ to $6 × 10^{-4}$ mS cm$^{-1}$ for temperatures from 450 to 275 °C.[36] It is therefore unsurprising that significant Na dynamics are not observed over the much lower temperature range investigated here, which is also the relevant temperature range for most Li-ion battery applications.

**Characterization of NaNb₁₃O₃₃ as a Battery Electrode Material.** Bond-valence sum energy (BVSE) mapping was performed on $NaNb_{13}O_{33}$ to approximate its Li- and Na-ion diffusion pathways and thus its performance as a host material for Li- and Na-ion battery applications. BVSE is a simple electrostatic method that uses the bond valence site energy approach to estimate the energy barriers relevant to ion diffusion within a crystal structure.[69] In this method, a mobile cation is chosen (here, $Li^+$ or $Na^+$), and the interaction energy between this ion and the entire structure, except for other ions of the same type, is calculated over a grid of locations throughout the structure. The resulting array of BVSE energies provides an estimation of relative hopping energy barriers, a representation of the energy landscape for the mobile ion, and a picture of conduction pathways.[21,51−53,70,71] The energy isosurface for $\Delta v = 0.1$ valence units is displayed for $NaNb_{13}O_{33}$ with $Li^+$ and $Na^+$ as mobile ions in Figure 3, where $\Delta v$ is the half-width (in valence units) of the volume accessible to the mobile ion.[69] From the extensive $Li^+$ conduction pathways visible at this cutoff, BVSE suggests low-energy barriers for intrablock hopping in the ac plane as well as low-energy-barrier pathways down the b axis within the blocks (Figure 3a,c). This combination of facile 1D diffusion down block channels and intrablock Li redistribution is consistent with previous studies of Wadsley−Roth Li diffusion mechanisms, and it has been credited for their Li diffusion coefficients on par with those of solid electrolyte materials.[18,19,29−31] Conversely, BVSE does not predict facile $Na^+$ hopping within octahedral blocks or down channels (Figure 3b,d). The only predicted low-energy-barrier $Na^+$ motion is localized within each $NbO_6$ cage and existing square-planar sites, suggesting that $NaNb_{13}O_{33}$ would make a poor Na-ion conductor.

Electronic structure calculations of the relaxed structure, starting from the model refined from 20 K neutron diffraction data, show a band diagram consisting of both flat and dispersive energy bands (Figure 4). Previous computational studies of similar Wadsley−Roth compounds have shown each $n × m$ block capable of holding one localized electron in Nb d-
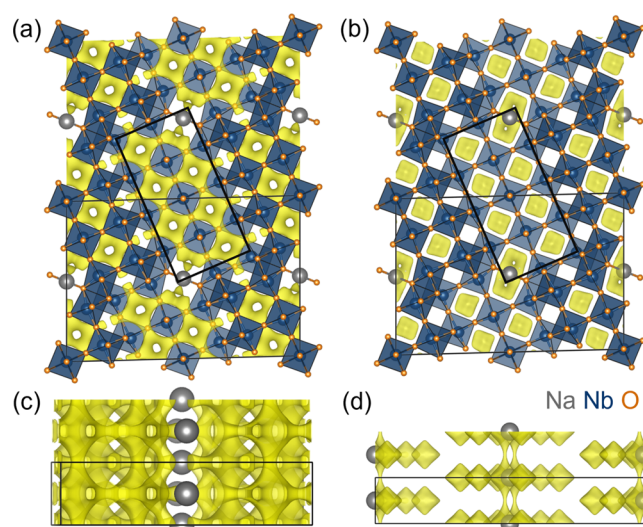


**Figure 3.** Bond-valence sum energy map of $Li^+$ (a, c) and $Na^+$ (b, d) as mobile ions in ordered $NaNb_{13}O_{33}$ viewed in the ac plane (top) and the ab plane (bottom). Low-energy-barrier Li-ion conduction pathways ($\Delta v = 0.1$ valence units) are shown in yellow.
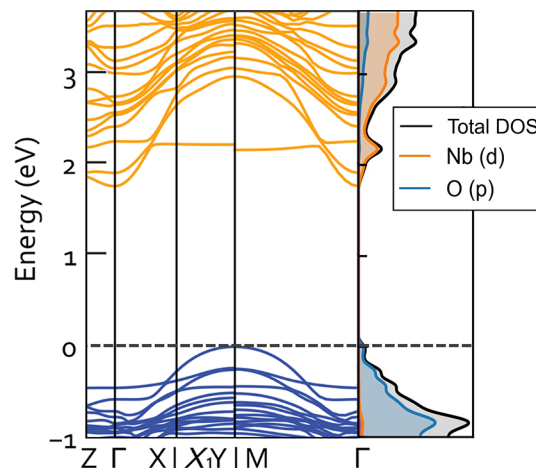


**Figure 4.** Band structure and density of states for $NaNb_{13}O_{33}$ calculated from the structure model from refinement of 1-NNO NPD obtained at 20 K. The Fermi level (dashed line) sits on top of the valence band.

orbitals dispersed over several octahedra.[26,72] These orbitals form a relatively flat band in the band diagram because the corner-sharing octahedra are too far apart to allow for extensive electron delocalization. Conversely, overlapping orbitals between edge-sharing octahedra create dispersive conduction bands. When the number of electrons per block exceeds unity, these latter states allow electron delocalization along the b-axis via the shear planes.[20,21,73] In the band structure of $NaNb_{13}O_{33}$, a relatively flat band is visible at the bottom of the conduction band (1.7−2.2 eV), indicating that electrons doping the structure from initial lithiation occupy such localized states as was seen with previous Wadsley−Roth compounds. With electron doping, the more dispersive bands beginning from 1.9 eV become accessible, suggesting electron delocalization along overlapping Nb d-orbitals and O p-orbitals in the shear planes. Experimental studies have demonstrated metallic conductivity along the shear planes when the one-electron-per-block threshold is exceeded.[18,29,74] Thus, n-

doping Wadsley–Roth phases with lithium insertion transform them from wide-band-gap insulators to good conductors. This insulator-to-metal transition as a function of lithiation has been observed at low lithium contents and obviates the need for nanostructuring or electron doping to achieve sufficient electronic conduction. From this band structure, we can therefore expect an insulator-to-metal transition and therefore good electronic conductivity as an electrode from $NaNb_{13}O_{33}$.

**Electrochemical Performance of $NaNb_{13}O_{33}$ in Li Cells.** Galvanostatic cycling of 2-NNO after three formation cycles at C/15 is shown in Figure 5a. Both the lithiation and



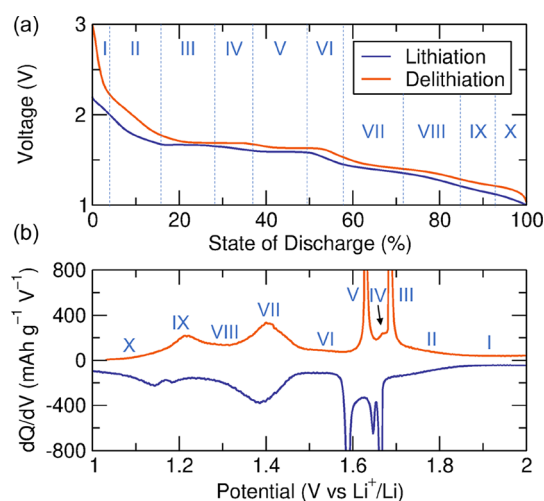**Figure 5.** Galvanostatic charge/discharge (GCD) profiles and differential capacity analysis of a $Li_xNaNb_{13}O_{33}$ vs Li cell after three C/15 formation cycles. (a) Galvanostatic profiles during lithiation and delithiation between 1 and 3 V vs Li$^+$/Li at a rate of C/15. (b) Corresponding dQ/dV vs V plot for the GCD curves in (a). Regions in (a) and the corresponding features in (b) are labeled with Roman numerals. The cell had an areal active material mass loading of approximately 2 mg cm$^{-2}$.

delithiation profiles exhibit at least ten different regions (labeled with Roman numerals), indicating a series of transitions between solid-solution and two-phase regions. To better identify these continuous and discontinuous phase transitions, we turned to differential capacity analysis (dQ/dV vs V). Figure 5b shows at least five peaks and four valleys. Each peak in the dQ/dV vs V plot suggests a phase transition that the active material undergoes during each lithiation and delithiation, with peaks in $NaNb_{13}O_{33}$ at 1.66 1.64, 1.58, 1.38, and 1.14 V vs Li$^+$/Li. The overpotential and capacity offset between lithiation and delithiation are both small, indicating high energy efficiency and high Coulombic reversibility, respectively (Figure 5a).

Symmetric rate capability was also characterized in $NaNb_{13}O_{33}$ half-cells (Figure 6) after three formation cycles at C/15. At 6C and 20C current densities, $NaNb_{13}O_{33}$ delivered 108 and 80 mAh g$^{-1}$ in approximately 5.4 and 1.2 min, respectively, indicating fast Li$^+$ insertion and extraction despite primary particles on the order of 1–10 μm (Figure S4 inset). Furthermore, at higher active material mass loadings (5.5 mg cm$^{-2}$), $NaNb_{13}O_{33}$ still exhibited a specific capacity of 95 mAh g$^{-1}$ at 10 C (Figure S10). We note that the clear plateaus in the galvanostatic profiles and peaks in the dQ/dV curves are suppressed or merge at rates of 6C and above (Figure S11). The application of higher currents can lead to a
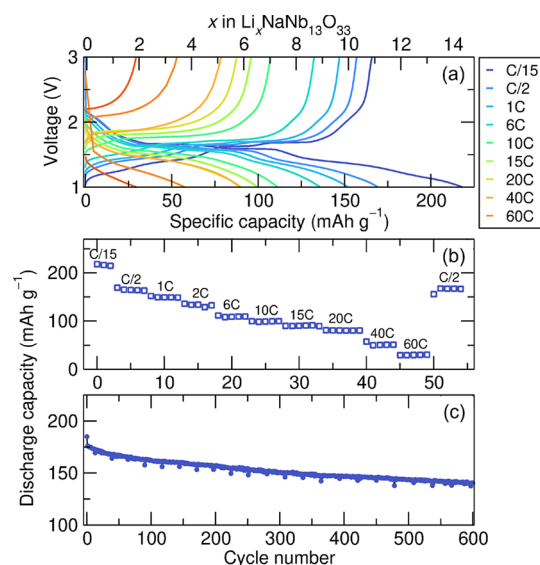


**Figure 6.** Rate performance of a $Li_xNaNb_{13}O_{33}$//Li cell with an areal active material mass loading of 2 mg cm$^{-2}$. (a) Representative galvanostatic charge–discharge curves at various C-rates after three formation cycles at C/15. (b) Specific capacities from (a) as a function of cycle number with increments in C-rate. (c) Specific capacity as a function of cycle number. Long-term cycling between 1 and 3 V was performed at a rate of 2C following two formation cycles at a rate of C/10.

nonequilibrium distribution of lithium through the electrode and/or individual particles, resulting in the coexistence of phases as indicated by the increasing width and decreasing height and area of the dQ/dV peaks (Figure S12). Increasing polarization with increasing current density is captured in the shifting dQ/dV peak locations. As a result, charge and discharge cutoff voltages are prematurely reached without achieving full removal or insertion of lithium (Figure S12a,e). These shifts in polarization are symmetric across lithiation and delithiation, indicating that ohmic and faradaic losses are similar during charge and discharge in this material.

Based on the above analysis, long-term cycling of lithium in $NaNb_{13}O_{33}$ half-cells from 1 to 3 V vs Li$^+$/Li was conducted at a charge/discharge rate of 2C after two C/10 formation cycles. After 600 cycles, the material shows 80% capacity retention (Figure 6c). As the number of cycles increases, the electrochemical features are not as pronounced compared to those of the first few cycles (Figures S13 and S14). This suggests a material transformation such as decreased long-range order or increased heterogeneity upon cycling. We note that the cycled cells experienced periodic temperature fluctuations, which accounts for the outliers in discharge capacity. We also note that no attempts were made to optimize this electrochemical performance, although it could likely be further improved through, e.g., calendering, conductive carbon network optimization, or electrolyte optimization.

The state-of-the-art high-rate lithium-ion battery anode material is lithium titanate spinel $Li_4Ti_5O_{12}$ (LTO). Based on a three-electron reduction to $Li_7Ti_5O_{12}$, the gravimetric capacity of lithium titanate is 175.1 mAh g$^{-1}$.[75] However, bulk $Li_4Ti_5O_{12}$ does not function well as an anode material and must be carbon-coated and nanoscaled to achieve high-rate (de)intercalation.[75,76] These synthetic modifications add cost and complexity to the manufacturing process, while nanoparticles show decreased packing density and enhanced side

reactions between the electrode particle surfaces and the electrolyte.[77] Additionally, LTO contains a large quantity of inactive lithium, which is disadvantageous in terms of resource utilization and because the price of lithium has seen a multifold increase in recent years. Wadsley—Roth phases have become well-known for their ability to rapidly store large quantities of lithium (above 200 mAh g$^{-1}$, beyond one Li per transition metal) even in micrometer-scale particles and in the absence of carbon coating.[18−20] Generally, only 3/5 of the Ti$^{4+}$ is reduced in Li$_4$Ti$_5$O$_{12}$ while Wadsley—Roth phases see full one-electron or multielectron redox, leading to higher gravimetric and volumetric capacities in the latter phases. The initial results on bulk NaNb$_{13}$O$_{33}$ show that it is capable of lithium storage in excess of 200 mA h g$^{-1}$ and retains about 50% capacity in a 5 min discharge relative to its 15 h discharge. Nonetheless, the maximum low-rate capacity and the high-rate capacity retention are lower than those observed in Wadsley—Roth phases such as TiNb$_2$O$_7$ and Nb$_{16}$W$_5$O$_{55}$. Additional electrochemical testing under optimized and standardized conditions would be warranted to consider the commercial applicability of NaNb$_{13}$O$_{33}$ as a high-rate oxide anode. Synthetic modifications such as doping and/or carbon coating could be pursued to improve the electronic conductivity and enhance the rate performance by minimizing ohmic losses observed at high current densities (Figure 6a).

Electrochemical sodiation of 2-NNO electrodes was also attempted. NaNb$_{13}$O$_{33}$ half-cells vs Na metal were cycled at rates from C/10 to C/100. As predicted by variable-temperature NMR and BVSE mappings, little to no sodium intercalation was observed (Figure S15). The calculated sodium hopping barriers in related Wadsley—Roth phases are extremely high.[29] It appears that the channel sizes and inflexibility of the framework are well-suited for rapid and reversible lithium intercalation but effectively hinder sodium conduction.

## CONCLUSION

Like many Wadsley—Roth phases, NaNb$_{13}$O$_{33}$ displays excellent lithium storage capacity that is largely maintained at high rates and over long-term cycling, even with micrometer-scale particles. Combined X-ray and neutron diffraction and $^{23}$Na solid-state NMR spectroscopy reveal that this Wadsley—Roth-like structure contains vacancies on the square-planar sodium site and that some sodium is present in the perovskite-like sites inside the 5 × 3 octahedral blocks of NaNb$_{13}$O$_{33}$. Reduction of Nb from the 5+ to the 4+ and partially to the 3+ oxidation state enables large lithium capacities, which do not seem inhibited by the presence of Na point defects in the block interiors, although the precise effects of this Na disorder on Li conduction were not investigated. Future studies might attempt to minimize the extent of this disorder, perhaps through lower-temperature synthesis techniques, and this should be easily quantifiable with $^{23}$Na solid-state NMR. Bond valence mapping suggests fast, quasi-1D Li diffusion down parallel block channels and facile hopping between neighboring channels, which explains the excellent rate performance observed (e.g., 100 mA h g$^{-1}$ at 20 C) despite the presence of tunnel blockages and large particle sizes. DFT electronic structure calculations are consistent with previous studies and suggest that there will be good electronic conductivity primarily along overlapping niobium d-orbitals and oxygen p-orbitals within shear planes once NaNb$_{13}$O$_{33}$ is n-doped by Li insertion. Intercalation of Na was also tested,

but high Na hopping barriers prevented any significant electrochemical energy storage, in agreement with BVSE calculations. Altogether, this work provides structural and electrochemical insights into a promising new high-rate lithium-ion battery anode material and expands the use of Wadsley—Roth battery materials into new compositional and structural phase space.

## ASSOCIATED CONTENT

### ⓢ Supporting Information

The Supporting Information is available free of charge at https://pubs.acs.org/doi/10.1021/acs.chemmater.3c01066.

> X-ray and neutron diffraction Rietveld fits, nuclear magnetic resonance spectra and scanning electron micrographs of pristine NaNb$_{13}$O$_{33}$ samples, X-ray diffraction of NaNbO$_3$ used for NMR analysis, NMR and X-ray diffraction supporting phase mapping, variable-temperature $^{23}$Na NMR spectra, Fourier difference map of NaNb$_{13}$O$_{33}$, and additional galvanostatic cycling data, including representative d$Q$/d$V$ curves and analysis and sodium half-cell cycling (PDF)

> Crystallographic information file of Na$_x$Nb$_{13}$O$_{33}$ at 300 K (NB: sodium occupancies were refined freely to test the model stability and thus do not sum precisely to NaNb$_{13}$O$_{33}$; see main text for details) (CIF)

> Crystallographic information file of Na$_x$Nb$_{13}$O$_{33}$ at 20 K (NB: sodium occupancies were refined freely to test the model stability and thus do not sum precisely to NaNb$_{13}$O$_{33}$; see main text for details) (CIF)

## AUTHOR INFORMATION

### Corresponding Author

**Kent J. Griffith** − *Department of Chemistry and Department of Materials Science and Engineering, Northwestern University, Evanston, Illinois 60208, United States;* ⓞ orcid.org/0000-0002-8096-906X; Email: k3griffith@ucsd.edu

### Authors

**Ashlea R. Patterson** − *Materials Department and Materials Research Laboratory, University of California, Santa Barbara, Santa Barbara, California 93106, United States*

**Rodrigo Elizalde-Segovia** − *Department of Chemistry, University of Southern California, Los Angeles, California 90007, United States;* ⓞ orcid.org/0000-0002-4139-7986

**Kira E. Wyckoff** − *Materials Department and Materials Research Laboratory, University of California, Santa Barbara, Santa Barbara, California 93106, United States;* ⓞ orcid.org/0000-0003-4353-9447

**Arava Zohar** − *Materials Department and Materials Research Laboratory and California NanoSystems Institute, University of California, Santa Barbara, Santa Barbara, California 93106, United States;* ⓞ orcid.org/0000-0002-8292-5968

**Patrick P. Ding** − *Department of Chemistry, Northwestern University, Evanston, Illinois 60208, United States;* ⓞ orcid.org/0000-0002-9629-4597

**Wiley M. Turner** − *Department of Chemistry, Northwestern University, Evanston, Illinois 60208, United States*

**Kenneth R. Poeppelmeier** − *Department of Chemistry, Northwestern University, Evanston, Illinois 60208, United States;* ⓞ orcid.org/0000-0003-1655-9127

**Sri R. Narayan** — *Department of Chemistry, University of Southern California, Los Angeles, California 90007, United States;* ⓘ orcid.org/0000-0002-7259-3728

**Raphaële J. Clément** — *Materials Department and Materials Research Laboratory, University of California, Santa Barbara, Santa Barbara, California 93106, United States;* ⓘ orcid.org/0000-0002-3611-1162

**Ram Seshadri** — *Materials Department and Materials Research Laboratory, University of California, Santa Barbara, Santa Barbara, California 93106, United States;* ⓘ orcid.org/0000-0001-5858-4027

Complete contact information is available at:
https://pubs.acs.org/10.1021/acs.chemmater.3c01066

**Notes**

The authors declare the following competing financial interest(s): K.J.G. is a stakeholder in a start-up company commercializing niobium-based anode materials.

S.R.N.: Deceased May 24, 2023.

*Note*: Several days before the submission of this manuscript, a paper appeared that focused on the electrochemical performance of $NaNb_{13}O_{33}$.[78] In this work, the room-temperature and low-temperature performance of $NaNb_{13}O_{33}$ are studied in detail. The applied focus of that work differs from the fundamental crystal chemical questions addressed through combined high-resolution diffraction and solid-state NMR in the present study.

## REFERENCES

(1) Belharouak, I.; Sun, Y.-K.; Liu, J.; Amine, K. Li-$(Ni_{1/3}Co_{1/3}Mn_{1/3})O_2$ As a Suitable Cathode for High power Applications. *J. Power Sources* **2003**, *123*, 247−252.

(2) Itou, Y.; Ukyo, Y. Performance of $LiNiCoO_2$ Materials for Advanced Lithium-Ion Batteries. *J. Power Sources* **2005**, *146*, 39−44.

(3) Vetter, J.; Novák, P.; Wagner, M. R.; Veit, C.; Möller, K.-C.; Besenhard, J.; Winter, M.; Wohlfahrt-Mehrens, M.; Vogler, C.; Hammouche, A. Ageing Mechanisms in Lithium-Ion Batteries. *J. Power Sources* **2005**, *147*, 269−281.

(4) Aurbach, D.; Zinigrad, E.; Cohen, Y.; Teller, H. A Short Review of Failure Mechanisms of Lithium Metal and Lithiated Graphite Anodes in Liquid Electrolyte Solutions. *Solid State Ion.* **2002**, *148*, 405−416.

(5) Abraham, K. Directions in Secondary Lithium Battery Research and Development. *Electrochim. Acta* **1993**, *38*, 1233−1248.

(6) Han, J.-T.; Huang, Y.-H.; Goodenough, J. B. New Anode Framework for Rechargeable Lithium Batteries. *Chem. Mater.* **2011**, *23*, 2027−2029.

(7) Han, J.-T.; Goodenough, J. B. 3-V Full Cell Performance of Anode Framework $TiNb_2O_7$/Spinel $LiNi_{0.5}Mn_{1.5}O_4$. *Chem. Mater.* **2011**, *23*, 3404−3407.

(8) Magnéli, A. Structures of the $ReO_3$-Type with Recurrent Dislocations of Atoms: 'Homologous Series' of Molybdenum and Tungsten Oxides. *Acta Crystallogr.* **1953**, *6*, 495−500.

(9) Roth, R.; Wadsley, A. Mixed Oxides of Titanium and Niobium: the Crystal Structure of $TiNb_{24}O_{62}$ ($TiO_2·12Nb_2O_5$). *Acta Crystallogr.* **1965**, *18*, 724−730.

(10) Roth, R. S.; Wadsley, A. D. Multiple Phase Formation in the Binary System $Nb_2O_5–WO_3$. I. Preparation and Identification of Phases. *Acta Crystallogr.* **1965**, *19*, 26−32.

(11) Roth, R. S.; Wadsley, A. D. Multiple Phase Formation in the Binary System $Nb_2O_5–WO_3$. II. The Structure of the Monoclinic Phases $WNb_{12}O_{33}$ and $W_5Nb_{16}O_{55}$. *Acta Crystallogr.* **1965**, *19*, 32−38.

(12) Roth, R. S.; Wadsley, A. D. Multiple Phase Formation in the Binary System $Nb_2O_5–WO_3$. III. The Structures of the Tetragonal Phases $W_3Nb_{14}O_{44}$ and $W_8Nb_{18}O_{69}$. *Acta Crystallogr.* **1965**, *19*, 38−42.

(13) Roth, R. S.; Wadsley, A. D. Multiple Phase Formation in the Binary System $Nb_2O_5–WO_3$. IV. The Block Principle. *Acta Crystallogr.* **1965**, *19*, 42−47.

(14) Cava, R. J.; Murphy, D. W.; Zahurak, S. M. Lithium Insertion in Wadsley−Roth Phases Based on Niobium Oxide. *J. Electrochem. Soc.* **1983**, *130*, 2345.

(15) Cava, R. J.; Murphy, D. W.; Zahurak, S. M. Secondary Lithium Cells Employing Vanadium Tungsten Oxide Positive Electrodes. *J. Electrochem. Soc.* **1983**, *130*, 243−245.

(16) Cava, R.; Murphy, D.; Rietman, E.; Zahurak, S.; Barz, H. Lithium Insertion, Electrical Conductivity, and Chemical Substitution in Various Crystallographic Shear Structures. *Solid State Ion.* **1983**, *9*, 407−411.

(17) Griffith, K. J.; Senyshyn, A.; Grey, C. P. Structural Stability from Crystallographic Shear in $TiO_2−Nb_2O_5$ Phases: Cation Ordering and Lithiation Behavior of $TiNb_{24}O_{62}$. *Inorg. Chem.* **2017**, *56*, 4002−4010.

(18) Griffith, K. J.; Wiaderek, K. M.; Cibin, G.; Marbella, L. E.; Grey, C. P. Niobium Tungsten Oxides for High-Rate Lithium-Ion Energy Storage. *Nature* **2018**, *559*, 556−563.

(19) Griffith, K. J.; Grey, C. P. Superionic Lithium Intercalation through $2 \times 2$ nm$^2$ Columns in the Crystallographic Shear Phase $Nb_{18}W_8O_{69}$. *Chem. Mater.* **2020**, *32*, 3860−3868.

(20) Preefer, M. B.; Saber, M.; Wei, Q.; Bashian, N. H.; Bocarsly, J. D.; Zhang, W.; Lee, G.; Milam-Guerrero, J.; Howard, E. S.; Vincent,

R. C.; Melot, B. C.; Van der Ven, A.; Seshadri, R.; Dunn, B. S. Multielectron Redox and Insulator-to-Metal Transition upon Lithium Insertion in the Fast-Charging, Wadsley-Roth Phase $PNb_9O_{25}$. *Chem. Mater.* **2020**, *32*, 4553−4563.

(21) Wyckoff, K. E.; Robertson, D. D.; Preefer, M. B.; Teicher, S. M. L.; Bienz, J.; Kautzsch, L.; Mates, T. E.; Cooley, J. A.; Tolbert, S. H.; Seshadri, R. High-Capacity $Li^+$ Storage through Multielectron Redox in the Fast-Charging Wadsley-Roth Phase $(W_{0.2}V_{0.8})_3O_7$. *Chem. Mater.* **2020**, *32*, 9415−9424.

(22) McColl, K.; Griffith, K. J.; Dally, R. L.; Li, R.; Douglas, J. E.; Poeppelmeier, K. R.; Corà, F.; Levin, I.; Butala, M. M. Energy Storage Mechanisms in Vacancy-Ordered Wadsley−Roth Layered Niobates. *J. Mater. Chem. A* **2021**, *9*, 20006−20023.

(23) Bashian, N. H.; Preefer, M. B.; Milam-Guerrero, J.; Zak, J. J.; Sendi, C.; Ahsan, S. A.; Vincent, R. C.; Haiges, R.; See, K. A.; Seshadri, R.; Melot, B. C. Understanding the Role of Crystallographic Shear on the Electrochemical Behavior of Niobium Oxyfluorides. *J. Mater. Chem. A* **2020**, *8*, 12623−12632.

(24) McColl, K.; Cora, F. Fast Lithium-ion Conductivity in the 'Empty-Perovskite' n = 2 Ruddlesden−Popper-type Oxysulphide $Y_2Ti_2S_2O_5$. *J. Mater. Chem.* **2021**, *9*, 7068−7084.

(25) Cava, R. J.; Santoro, A.; Murphy, D.; Zahurak, S.; Roth, R. Structural Aspects of Lithium Insertion in Oxides: $Li_xReO_3$ and $Li_2FeV_3O_8$. *Solid State Ion.* **1981**, *5*, 323−326.

(26) Koçer, C. P.; Griffith, K. J.; Grey, C. P.; Morris, A. J. Cation Disorder and Lithium Insertion Mechanism of Wadsley−Roth Crystallographic Shear Phases from First Principles. *J. Am. Chem. Soc.* **2019**, *141*, 15121−15134.

(27) Vincent, R. C.; Cheetham, A. K.; Seshadri, R. Structure and Lithium Insertion in Oxides of Molybdenum. *APL. Mater.* **2023**, *11*, 010902.

(28) Parui, K.; Lee, A. D.; Gandhi, S.; Butala, M. M. R-$Nb_2O_5$ has an 'Idealized' $V_2O_5$ Structure and Wadsley−Roth-like Structural Stability during Li-ion Battery Cycling. *J. Mater. Chem.* **2023**, *11*, 5559−5567.

(29) Griffith, K. J.; Seymour, I. D.; Hope, M. A.; Butala, M. M.; Lamontagne, L. K.; Preefer, M. B.; Kocer, C. P.; Henkelman, G.; Morris, A. J.; Cliffe, M. J.; Dutton, S. E.; Grey, C. P. Ionic and Electronic Conduction in $TiNb_2O_7$. *J. Am. Chem. Soc.* **2019**, *141*, 16706−16725.

(30) Koçer, C. P.; Griffith, K. J.; Grey, C. P.; Morris, A. J. Lithium Diffusion in Niobium Tungsten Oxide Shear Structures. *Chem. Mater.* **2020**, *32*, 3980−3989.

(31) Liang, Z.; Xiang, Y.; Wang, D.; Fu, R.; Yang, Y. *NMR and MRI of Electrochemical Energy Storage Materials and Devices*; Royal Society of Chemistry: 2021.

(32) Cava, R.; Batlogg, B.; Krajewski, J.; Gammel, P.; Poulsen, H.; Peck, W.; Rupp, L. Antiferromagnetism and Metallic Conductivity in $Nb_{12}O_{29}$. *Nature* **1991**, *350*, 598−600.

(33) Cava, R.; Batlogg, B.; Krajewski, J.; Poulsen, H.; Gammel, P.; Peck, W., Jr.; Rupp, L., Jr. Electrical and Magnetic Properties of $Nb_2O_{5-\delta}$ Crystallographic Shear Structures. *Phys. Rev. B* **1991**, *44*, 6973.

(34) Ruscher, C.; Salje, E.; Hussain, A. The Effect of High Polaron Concentration on the Polaron Transport in $NbO_{2.5-x}$: Optical and Electrical Properties. *J. Phys. C: Solid State Phys.* **1988**, *21*, 3737.

(35) Andersson, S.; Selte, K.; Kjekshus, A.; Nielsen, P. H.; Sjöberg, B.; Larsen, E. The Crystal Structure of $NaNb_3O_{33}$ and the Geometrical Principles of the Homologous Series $NaM_{3n+1}O_{8n+1}$. *Acta Chem. Scand.* **1965**, *19*, 557.

(36) Bovin, J. O. Ionic Conductivity and the Conductivity-Blocking Defect Structure of $NaNb_{13}O_{33}$. *J. Solid State Chem.* **1984**, *54*, 277−281.

(37) Irle, E.; Blachnik, R.; Gather, B. The Phase Diagrams of $Na_2O$ and $K_2O$ with $Nb_2O_5$ and the Ternary System $Nb_2O_5−Na_2O−Yb_2O_3$. *Thermochim. Acta* **1991**, *179*, 157−169.

(38) Popovič, A.; Bencze, L.; Koruza, J.; Malič, B.; Kosec, M. Knudsen Effusion Mass Spectrometric Approach to the Thermodynamics of $Na_2O−Nb_2O_5$ system. *Int. J. Mass Spectrom.* **2012**, *309*, 70−78.

(39) Appendino, P. Contributo Allo Studio del Sistema $Na_2O-Nb_2O_5$. *Ann. Chim. Ital.* **1973**, *63*, 277−281.

(40) Huq, A.; Kirkham, M.; Peterson, P. F.; Hodges, J. P.; Whitfield, P. S.; Page, K.; Hugle, T.; Iverson, E. B.; Parizzi, A.; Rennich, G. POWGEN: Rebuild of a Third-Generation Powder Diffractometer at the Spallation Neutron Source. *J. Appl. Crystallogr.* **2019**, *52*, 1189−1201.

(41) Toby, B. H.; Von Dreele, R. B. GSAS-II: The Genesis of a Modern Open-Source all Purpose Crystallography Software PAckage. *J. Appl. Crystallogr.* **2013**, *46*, 544−549.

(42) Bielecki, A.; Burum, D. P. Temperature Dependence of $^{207}Pb$ MAS Spectra of Solid Lead Nitrate. An Accurate, Sensitive Thermometer for Variable-Temperature MAS. *J. Magn. Reson.* **1995**, *116*, 215−220.

(43) Beckmann, P. A.; Dybowski, C. A Thermometer for Nonspinning Solid-State NMR Spectroscopy. *J. Magn. Reson.* **2000**, *146*, 379−380.

(44) Kresse, G.; Hafner, J. Ab Initio Molecular Dynamics for Liquid metals. *Phys. Rev. B* **1993**, *47*, 558.

(45) Kresse, G.; Furthmüller, J. Efficiency of Ab-Initio Total Energy Calculations for Metals and Semiconductors Using a Plane-Wave Basis Set. *Comput. Mater. Sci.* **1996**, *6*, 15−50.

(46) Kresse, G.; Furthmüller, J. Efficient Iterative Schemes for Ab Initio Total-Energy Calculations Using a Plane-Wave Basis Set. *Phys. Rev. B* **1996**, *54*, 11169.

(47) Kresse, G.; Hafner, J. Norm-Conserving and Ultrasoft Pseudopotentials for First-Row and Transition Elements. *J. Condens. Matter Phys.* **1994**, *6*, 8245.

(48) Kresse, G.; Joubert, D. From Ultrasoft Pseudopotentials to the Projector Augmented-Wave Method. *Phys. Rev. B* **1999**, *59*, 1758.

(49) Perdew, J. P.; Burke, K.; Ernzerhof, M. Generalized Gradient Approximation Made Simple. *Phys. Rev. Lett.* **1996**, *77*, 3865.

(50) Ganose, A. M.; Jackson, A. J.; Scanlon, D. O. SUMO: Command-Line Tools for Plotting and Analysis of Periodic *Ab Initio* Calculations. *J. Open Source Softw.* **2018**, *3*, 717.

(51) Chen, H.; Wong, L. L.; Adams, S. SoftBV−A Software Tool for Screening the Materials Genome of Inorganic Fast Ion Conductors. *Acta Crystallogr. B Struct.* **2019**, *75*, 18−33.

(52) Chen, H.; Adams, S. Bond Softness Sensitive Bond-Valence Parameters for Crystal Structure Plausibility Tests. *IUCrJ.* **2017**, *4*, 614−625.

(53) Wong, L. L.; Phuah, K. C.; Dai, R.; Chen, H.; Chew, W. S.; Adams, S. Bond Valence Pathway Analyzer—An Automatic Rapid Screening Tool for Fast Ion Conductors within softBV. *Chem. Mater.* **2021**, *33*, 625−641.

(54) Momma, K.; Izumi, F. VESTA 3 for Three-dimensional Visualization of Crystal, Volumetric and Morphology Data. *J. Appl. Crystallogr.* **2011**, *44*, 1272−1276.

(55) Clark, S. J.; Segall, M. D.; Pickard, C. J.; Hasnip, P. J.; Probert, M. I.; Refson, K.; Payne, M. C. First Principles Methods Using CASTEP. *Z. Kristallogr.* **2005**, *220*, 567−570.

(56) Vanderbilt, D. Soft Self-Consistent Pseudopotentials in a Generalized Eigenvalue Formalism. *Phys. Rev. B* **1990**, *41*, 7892.

(57) Perdew, J. P.; Burke, K.; Ernzerhof, M. Generalized Gradient Approximation Made Simple. *Phys. Rev. Lett.* **1996**, *77*, 3865.

(58) Monkhorst, H. J.; Pack, J. D. Special Points for Brillouin-zone Integrations. *Phys. Rev. B* **1976**, *13*, 5188.

(59) Pickard, C. J.; Mauri, F. All-Electron Magnetic Response with Pseudopotentials: NMR Chemical Shifts. *Phys. Rev. B* **2001**, *63*, 245101.

(60) Yates, J. R.; Pickard, C. J.; Mauri, F. Calculation of NMR Chemical Shifts for Extended Systems Using Ultrasoft Pseudopotentials. *Phys. Rev. B* **2007**, *76*, No. 024401.

(61) Profeta, M.; Mauri, F.; Pickard, C. J. Accurate First Principles Prediction of $^{17}O$ NMR Parameters in $SiO_2$: Assignment of the Zeolite Ferrierite Spectrum. *J. Am. Chem. Soc.* **2003**, *125*, 541−548.

(62) Ashbrook, S. E.; Le Polles, L.; Gautier, R.; Pickard, C. J.; Walton, R. I. $^{23}Na$ Multiple-Quantum MAS NMR of the Perovskites $NaNbO_3$ and $NaTaO_3$. *Phys. Chem. Chem. Phys.* **2006**, *8*, 3423−3431.

(63) Johnston, K. E.; Tang, C. C.; Parker, J. E.; Knight, K. S.; Lightfoot, P.; Ashbrook, S. E. The Polar Phase of NaNbO$_3$: A Combined Study by Powder Diffraction, Solid-State NMR, and First-Principles Calculations. *J. Am. Chem. Soc.* **2010**, *132*, 8732−8746.

(64) Seidel, P.; Hoffmann, W. Verfeinerung der Kristallstruktur von NaNbO$_3$ N. Bestimmung der Absoluten Konfiguration und des Zwillingsgesetzes. *Z. Kristallogr.* **1976**, *143*, 444−459.

(65) Alemany, L. B.; Massiot, D.; Sherriff, B. L.; Smith, M. E.; Taulelle, F. Observation and Accurate Quantification of $^{27}$Al MAS NMR Spectra of Some Al$_2$SiO$_5$ Polymorphs Containing Sites with Large Quadrupole Interactions. *Chem. Phys. Lett.* **1991**, *177*, No. 301−306.

(66) Eden, M. *Annual Reports on NMR Spectroscopy*; Elsevier: 2020; Vol. *101*, pp 285−410.

(67) Ohno, S.; Imasato, K.; Anand, S.; Tamaki, H.; Kang, S. D.; Gorai, P.; Sato, H. K.; Toberer, E. S.; Kanno, T.; Snyder, G. J. Phase Boundary Mapping to Obtain n-type Mg$_3$Sb$_2$ -Based Thermoelectrics. *Joule* **2018**, *2*, 141−154.

(68) Jood, P.; Male, J. P.; Anand, S.; Matsushita, Y.; Takagiwa, Y.; Kanatzidis, M. G.; Snyder, G. J.; Ohta, M. Na Doping in PbTe: Solubility, Band Convergence, Phase Boundary Mapping, and Thermoelectric Properties. *J. Am. Chem. Soc.* **2020**, *142*, 15464−15475.

(69) Brown, I. D. Recent Developments in the Methods and Applications of the Bond Valence Model. *Chem. Rev.* **2009**, *109*, 6858−6919.

(70) Avdeev, M.; Sale, M.; Adams, S.; Rao, R. P. Screening of the Alkali-metal Ion Containing Materials from the Inorganic Crystal Structure Database (ICSD) for High Ionic Conductivity Pathways using the Bond Valence Method. *Solid State Ion.* **2012**, *225*, 43−46.

(71) Xiao, R.; Li, H.; Chen, L. High-throughput Design and Optimization of Fast Lithium Ion Conductors by the Combination of Bond-valence Method and Density Functional Theory. *Sci. Rep.* **2015**, *5*, 14227.

(72) Koçer, C. P.; Griffith, K. J.; Grey, C. P.; Morris, A. J. First-principles Study of Localized and Delocalized Electronic States in Crystallographic Shear Phases of Niobium Oxide. *Phys. Rev. B* **2019**, *99*, 075151.

(73) Saber, M.; Preefer, M. B.; Kolli, S. K.; Zhang, W.; Laurita, G.; Dunn, B.; Seshadri, R.; Van der Ven, A. Role of Electronic Structure in Li Ordering and Chemical Strain in the Fast Charging Wadsley−Roth Phase PNb$_9$O$_{25}$. *Chem. Mater.* **2021**, *33*, 7755−7766.

(74) Kocer, C. First-Principles Studies of Complex Oxide Materials. Ph.D. Thesis, University of Cambridge, 2021.

(75) Shen, L.; Zhang, X.; Uchaker, E.; Yuan, C.; Cao, G. Li$_4$Ti$_5$O$_{12}$ Nanoparticles Embedded in a Mesoporous Carbon Matrix as a Superior Anode Material for High Rate Lithium Ion Batteries. *Adv. Energy Mater.* **2012**, *2*, 691−698.

(76) Prakash, A.; Manikandan, P.; Ramesha, K.; Sathiya, M.; Tarascon, J.; Shukla, A. Solution-combustion Synthesized Nano-crystalline Li$_4$Ti$_5$O$_{12}$ as High-rate Performance Li-ion Battery Anode. *Chem. Mater.* **2010**, *22*, 2857−2863.

(77) Yuan, T.; Tan, Z.; Ma, C.; Yang, J.; Ma, Z.-F.; Zheng, S. Challenges of Spinel Li$_4$Ti$_5$O$_{12}$ for Lithium-ion Battery Industrial Applications. *Adv. Energy Mater.* **2017**, *7*, 1601625.

(78) Gao, J.; et al. Sodium Niobate with a Large Interlayer Spacing: A Fast-Charging, Long-Life, and Low-Temperature Friendly Lithium-Storage Material. *Advanced Science* **2023**, *10*, 2300583.